Supporting Information

Heteroatom-Doped Carbon Interpenetrating Networks：A Signpost to Achieve the Best Performance of Non-PGM Catalysts for Fuel Cells

Lu Bai, Jingjun Liu*, Chun Jin, Jin Zhang and Feng Wang*

L. Bai, Prof. J. Liu, C. Jin, J. Zhang and Prof. F. Wang

State Key Laboratory of Chemical Resource Engineering; Beijing Key Laboratory of

Electrochemical Process and Technology for Materials, Beijing University of Chemical

Technology, Beijing, 100029, PR China

*E-mail: liujingjun@mail.buct.edu.cn (Jingjun Liu)
*E-mail: wangf@mail.buct.edu.cn (Feng Wang)
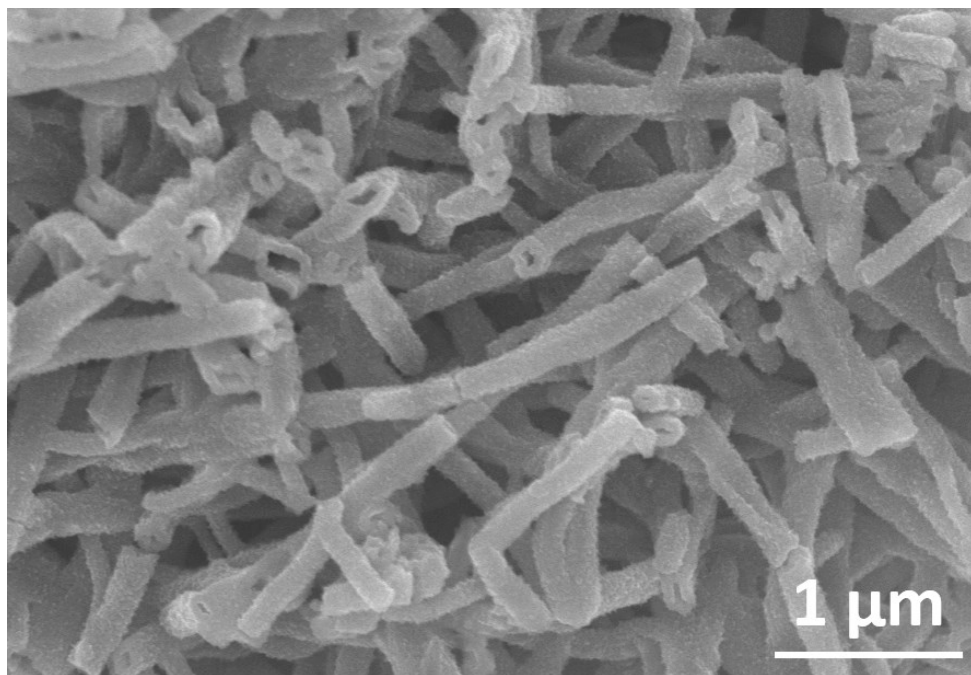
Tel: +86-10-64411301

Captions
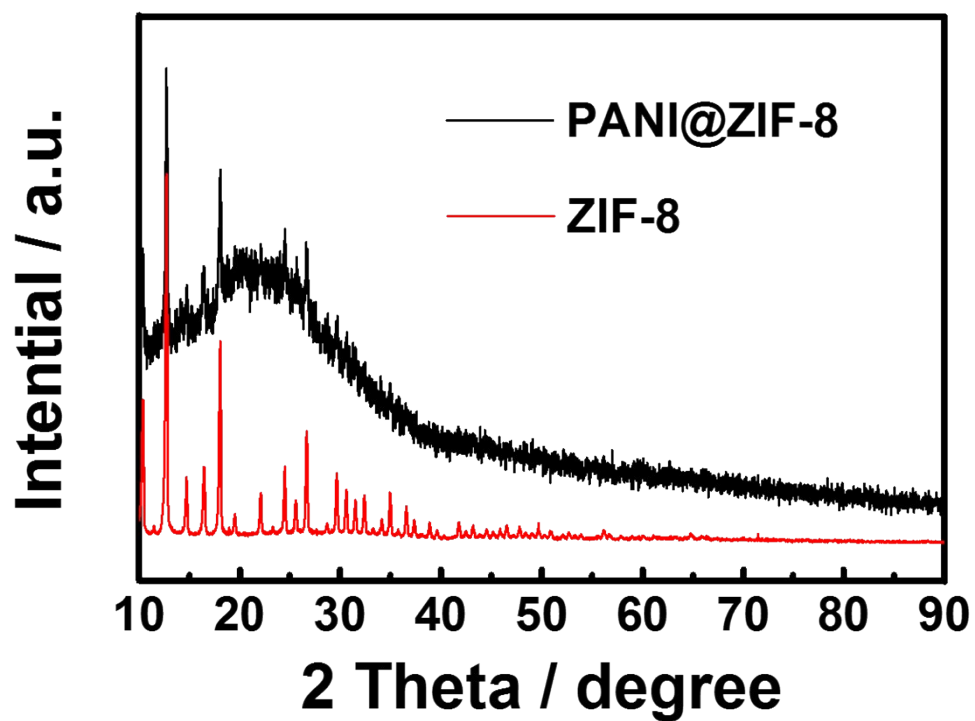

Figure S1. SEM image of PANI.

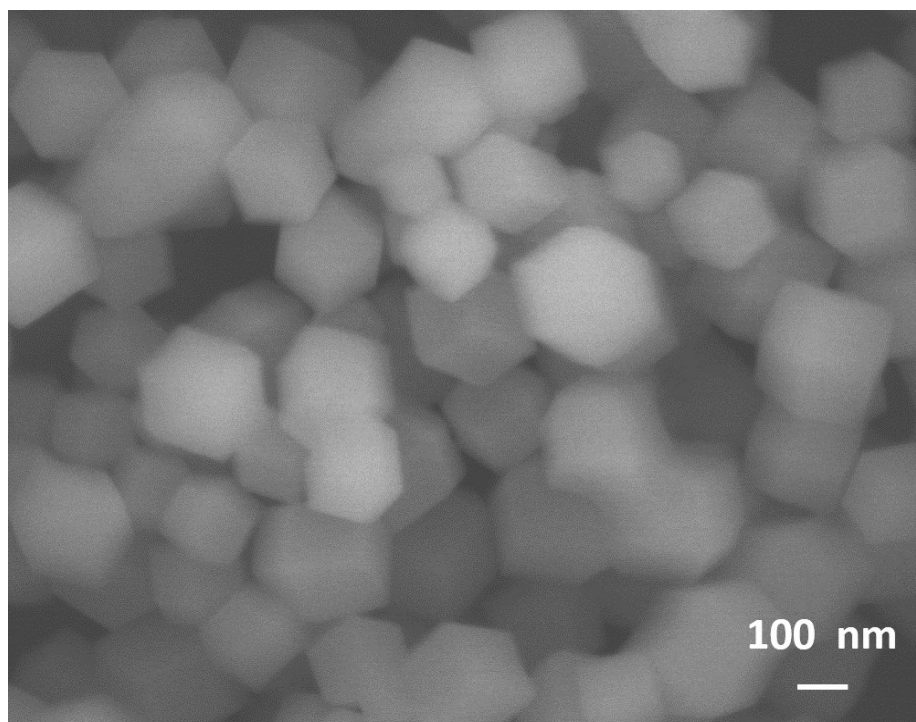**Figure S2**. XRD spectra of PANI@ZIF-8 and ZIF-8.
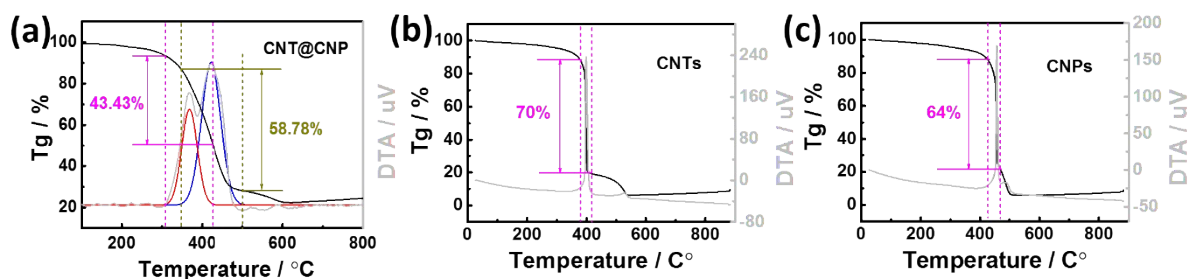
Figure S3. SEM image for ZIF-8.

Figure S4. TG and DTA curves for (a) CNT@CNP interpenetrating networks; (b) CNTs; (c) CNPs in the air atmosphere.

From the weight loss curve shown in Figure S4(a), the hybrid sample shows two distinct downturns compared with that of CNTs (Figure S4(b)) and CNPs (Figure S4(c)). The specific weight loss of CNTs and CNPs are 70% and 64% respectively measured by TG test. In addition, the DTA method was operated to obtain a temporary increase or decrease of a standard object when any chemical or physical change in an unknown compound, in this case, the decrease is endothermic and the increase is exothermic. The obvious two exothermic peaks have occurred

3

around 380 and 420°C respectively as shown in Figure S4(a), which indicates at least two compounds with different oxidized reaction temperature. However, the CNTs and CNPs show a monomer phase structure due to their single sharp peak. The exothermic temperature of them above are 400 and 450°C, which are closely to the positions of these temperature in DTA result of the hybrid, which further proof the existence of two carbon phases in the CNT@CNP. Based on the temperature and weight loss value of CNTs and CNPs performed by TG-DTA, we can get the rate of two partial contents in hybrid product. The two fitting peaks represent the CNTs and CNPs existed in CNT@CNP with relative contents of 43.43% and 58.78%, respectively.
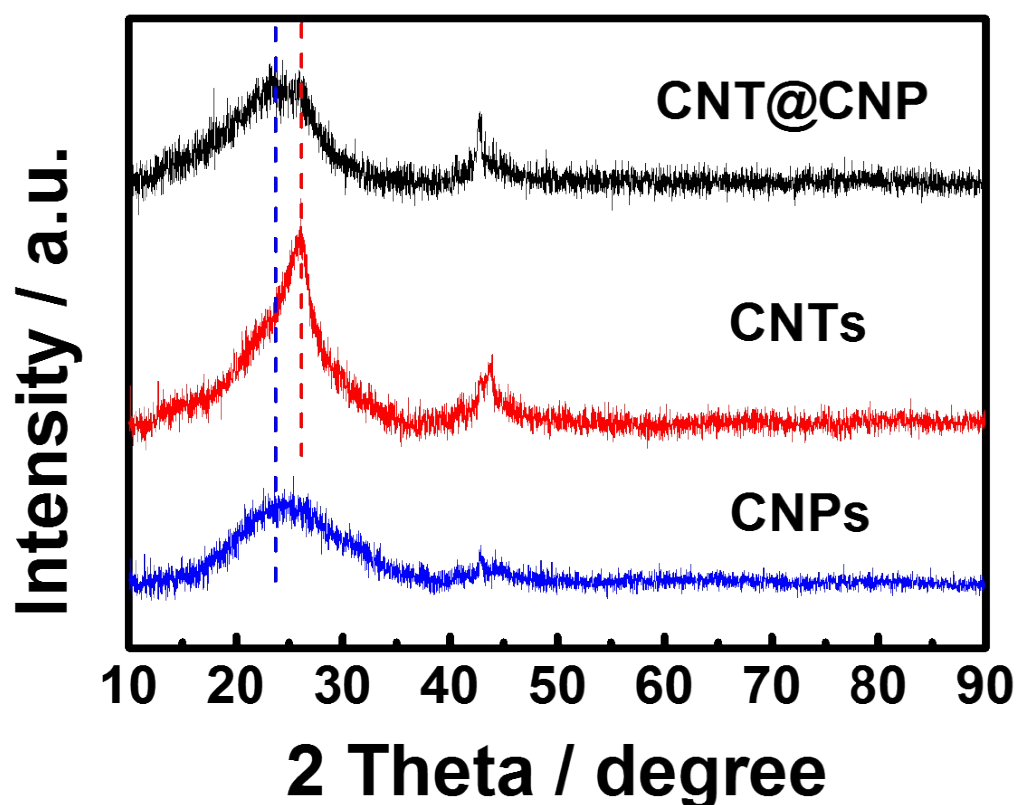

Figure S5. XRD curves for CNT@CNP interpenetrating networks, CNTs and CNPs, respectively.
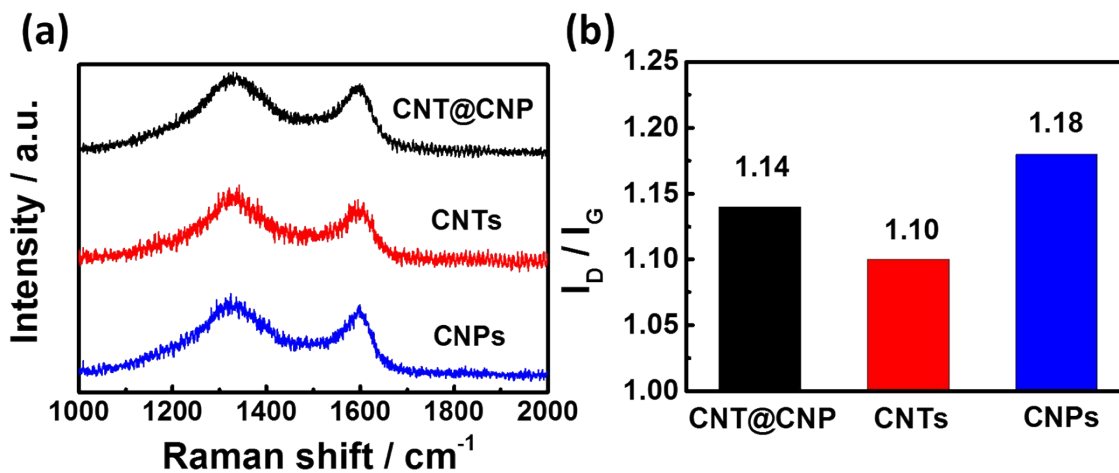
Figure S6. (a) Raman curves and (b) I_D/I_G values of CNT@CNP interpenetrating networks, CNTs and CNPs, respectively.

Structural information was operated by Raman spectroscopic measurement. two pronounced peaks of the characteristic D band at 1350 cm^{-1} and G band at 1590 cm^{-1} read from Raman spectra was shown in Figure S6. The D band is attributed to breaking of the symmetry caused by structural disorder and defects , while the G band is assigned to the graphitic E_{2g} mode corresponding to the in-plain bond-stretching motion of a pair of sp^2 carbon atoms.[1] The intensity ratio of the D band to the G band (I_D/I_G) is usually served as an indicator for evaluating the degree of disorder or defect in carbon materials. From the Raman spectra, the I_D/I_G values are estimated to be 1.10, 1.18 and 1.14 for CNTs, CNPs and CNT@CNP composite, respectively.
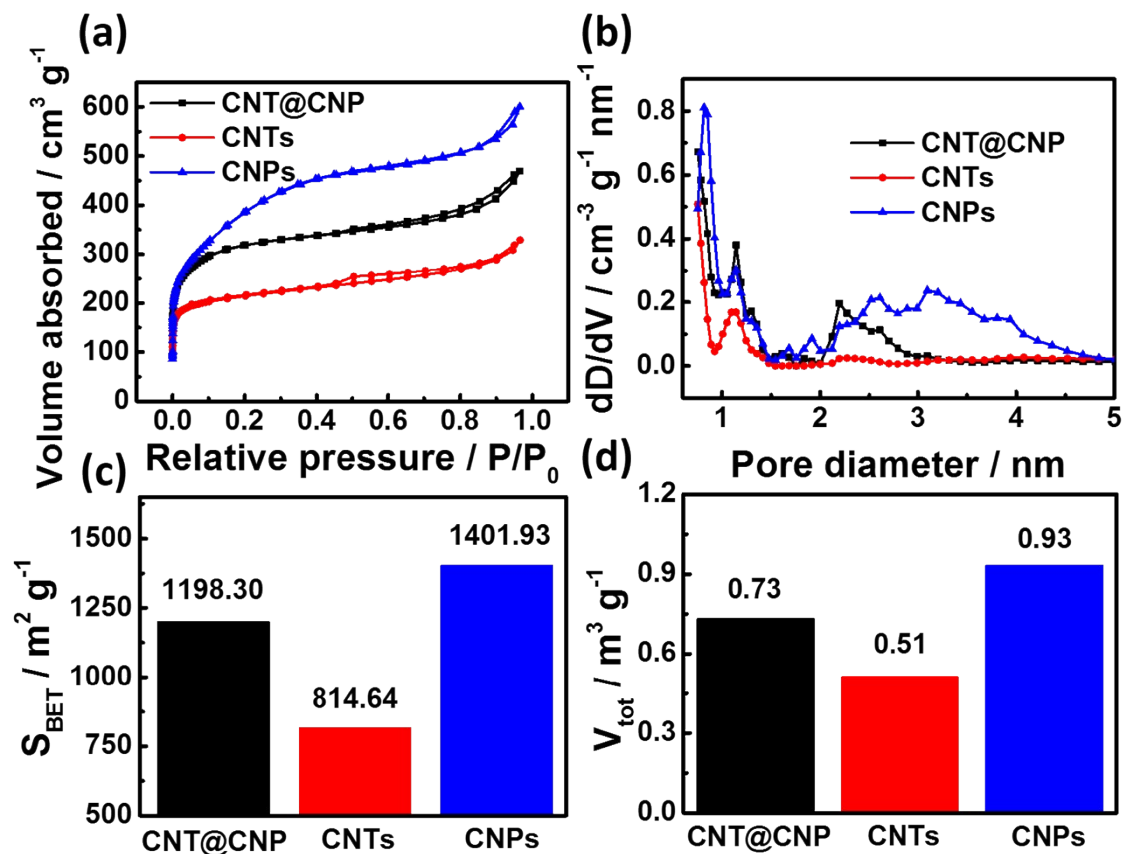
Figure S7. (a) N_2 adsorption-desorption isotherms and (b) Pore-size distributions as estimated by DFT method of CNT@CNP interpenetrating networks, CNTs and CNPs. (c) The specific surface area and (d) Pore volume for CNT@CNP, CNTs and CNPs, respectively.

The specific surface areas and pore size distribution for CNTs, CNPs and CNT@CNP samples were determined by nitrogen adsorption-desorption analyses at 77.3K presented in Figure S7(a). The recorded carbon products display a high speed uptake of nitrogen at low relative pressures ($P/P_0 < 0.001$), expressing abundant micropores in these samples. Moreover, a rapid rise in the nitrogen adsorption isotherms for the carbon materials were observed as well during high relative pressure ($< P/P_0$), accounting for the existence of mesopores and/or macropores in them, which are possibly owing to the inter-particle porosity or void.[2] No obvious hysteresis was observed for all the candidates probably owing to the rigidity of the framework skeleton after pyrolysis. The specific surface areas of CNTs, CNPs and CNT@CNP

composite determined by the BET method were 814.64, 1401.93 and 1198.30 m^2 g^{-1}, respectively as shown in Figure S7(c). The corresponding pore size distribution of CNTs, CNPs and dual carbons composite derived by BJH method clearly high intensity at the pore diameters smaller than 5 nm depicted in Figure S7(b), indicating the existence of abundant micropores (0.8 ~ 2 nm) and mesopores (2 ~ 50 nm). The pore volume of CNTs, CNPs and carbon/carbon hybrid are 0.51, 0.93 and 0.73 cm^3 g^{-1}, respectively shown in Figure S7(d). This result indicates that the surface morphology and porous feature of CNT@CNP composite are both lower than that of CNPs while higher than that of CNTs. Therefore, it is evidence of a dual carbon composite derived from CNTs and CNPs. The abundant pore structure of CNT@CNP may be attributed to the pyrolysis process, where unstable molecule gas (such as NH_3, CO) coming out from PANI fully contacted with capped ZIF-8. This special interior gas activation protect abundant microporous and mesoporous structure of ZIF-8 from collapsing and melting during the carbonated process with only NH_3 activation exterior, further increasing structure stability of CNT@CNP. Therefore a potential self-supported three dimension porous network structure is constructed to the benefit for proton and electron transfer.[3-4]
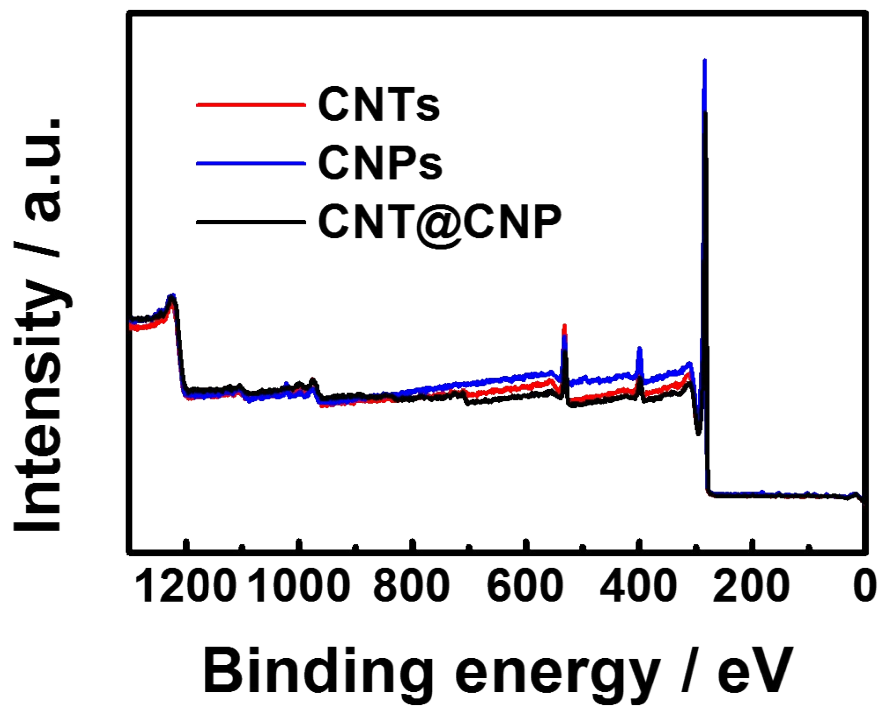
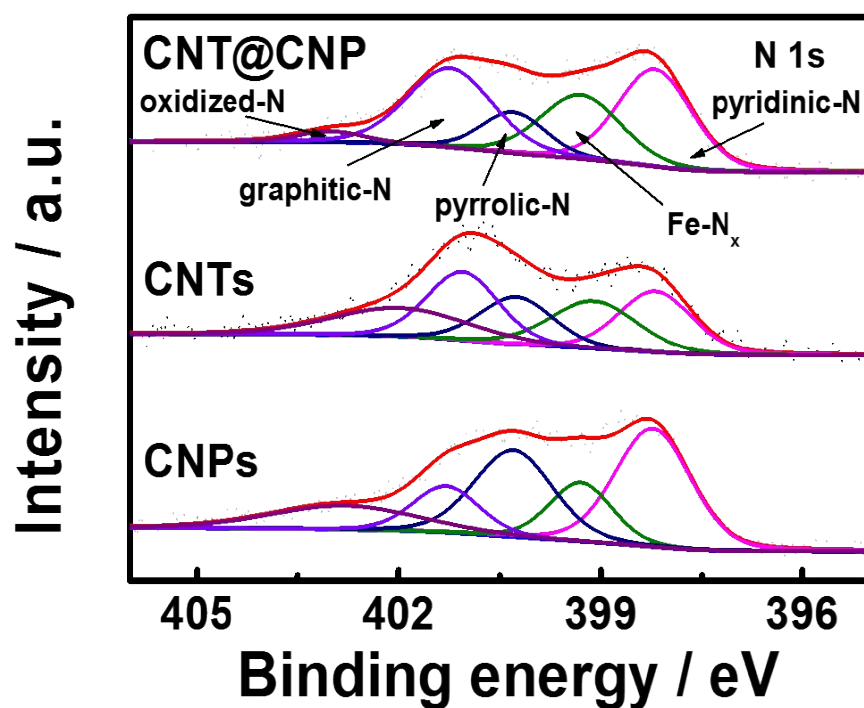**Figure S8.** XPS spectra surveys of CNT@CNP interpenetrating networks, CNTs and CNPs.

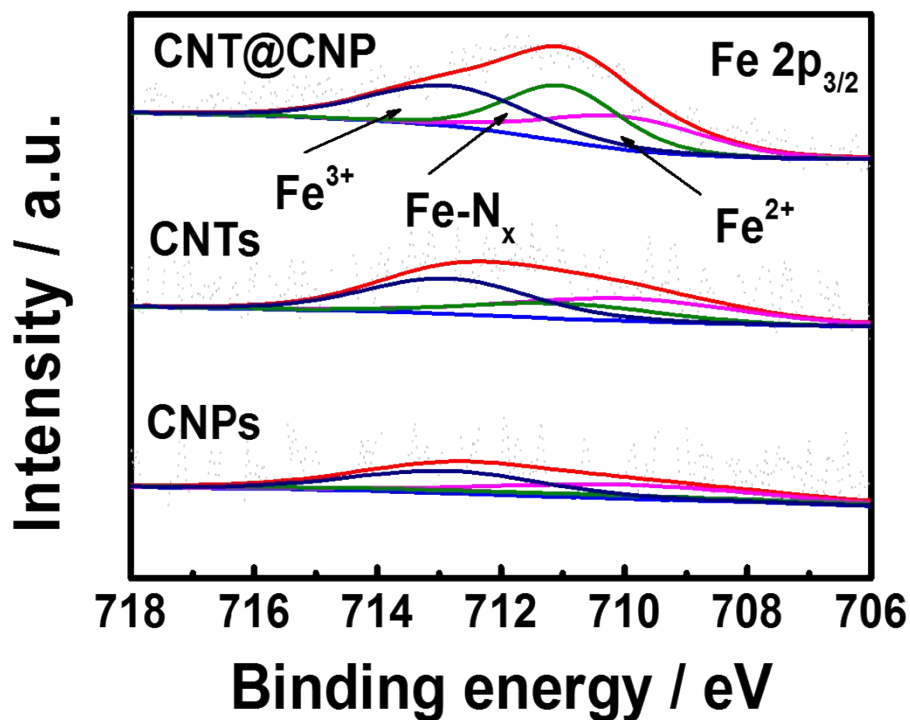

Figure S9. XPS spectra of N 1s.

Figure S10. Fe $2p_{3/2}$ for CNT@CNP interpenetrating networks, CNTs and CNPs.

The surface chemical states of the catalysts was examined by high-resolution XPS measurement on C 1s, N 1s, O 1s and Fe $2p_{3/2}$ peaks. High-resolution XPS C1s spectra present an asymmetric peak shape with the main component at 285 eV corresponding to the sp^2 hybridized graphitic carbon. For each of the above samples, the survey spectra give strong C, O, N and Fe signal as shown in Figure S8. The relative contents of these above elements are given in Table S2. The contents of the doped nitrogen species, referring to N/C unless other stated, in these samples are different: CNTs (4.76 at.%), CNPs (6.58 at.%) and CNT@CNP (5.32 at.%). The N 1s XPS spectra of these samples were fitted and the obtained result were shown in Figure S9. As observed, there are five peaks: pyridinic N (398.2 eV), Fe-N_x (399.3 eV), pyrrolic N (400.3 eV), graphitic N (401.3 eV) and oxidic N (403 eV).[5-6] The absolute content of various nitrogen states for CNTs, CNPs and CNT@CNP composite are quantitatively shown Figure 2(c) and table S3. In addition, for same amount of iron resource used in the above products, the contents of doped metal relative to carbon are different: CNTs

9

(0.19 at.%), CNPs (0.14 at.%) and CNT@CNP (0.28 at.%), respectively. The apparent Fe-N_x peak indicates the metal atom is bonded with N atoms to form Fe-N_x. the relative contents of which in CNTs, CNPs and duel carbons composite are 0.65, 0.89 and 1.10 at.%, respectively (Table S3). To further explore the structural configuration of the iron metal in these samples, the Fe $2p_{3/2}$ XPS spectra of these three products have been fitted and the result was depicted in Figure S9(b), where three main peaks were Fe^{2+} (712.85 eV), Fe-N_x (711 eV) and Fe^{3+} (710 eV).[7-8] The fitted result of Fe-N_x in above samples have been summarized in Table S4, where the relative contents are 0.04 at. % for CNTs, 0.02 at. % for CNPs and 0.09 at. % for carbon/carbon composite. These outcome results reveal that much more FeN_x existed in CNT@CNP composite. Furthermore, compared with CNTs and CNPs, the extra FeN_x part existed in dual carbon composite probably embedded into the interface, boundary and edge since high energy there. Based on the FeN_x contents from N1s and Fe $2p_{3/2}$ for CNTs, CNPs and CNT@CNP, the interfacial FeN_x content in dual carbon composite was calculated through the equation below:

$$n_{inter} = n_1 - n_2 - n_3 \qquad\qquad\qquad\qquad (S1)$$

Where n_{inter}, n_1, n_2, n_3 are served as contents of FeN_x in interface, CNT@CNP, CNTs and CNPs, respectively. According to the equation, the content of the interfacial FeN_x based on result from Fe $2p_{3/2}$ is 0.03 at. % (called n_{inter} (Fe_{2p})) and the value from N 1s outcome is 0.22 at. % (marked as n_{inter} (N_{1s})), where the occupied ratio of CNTs and CNPs is 44:56 derived from TG-DTA.
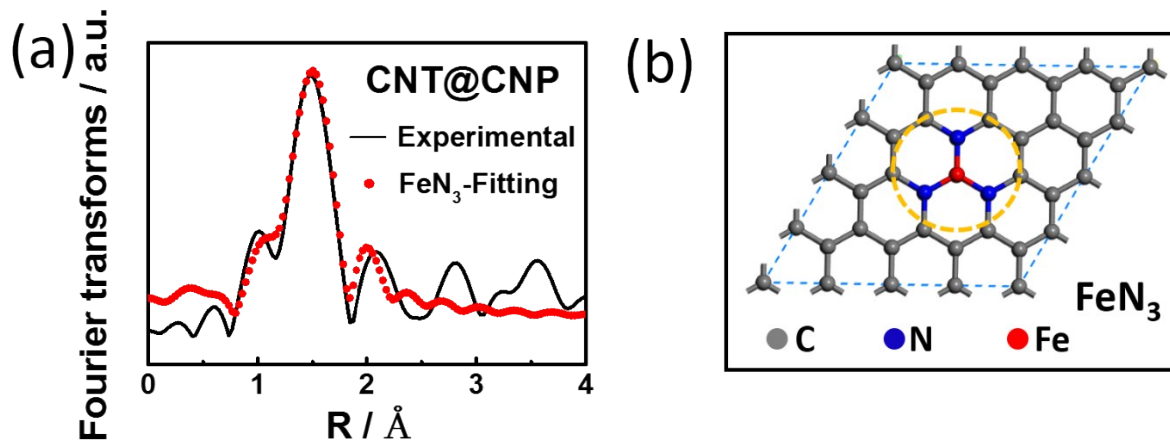
Figure S11. (a) The corresponding EXAFS R-space fitting curve of CNT@CNP and (b) Schematic atomic structure of FeN_3.
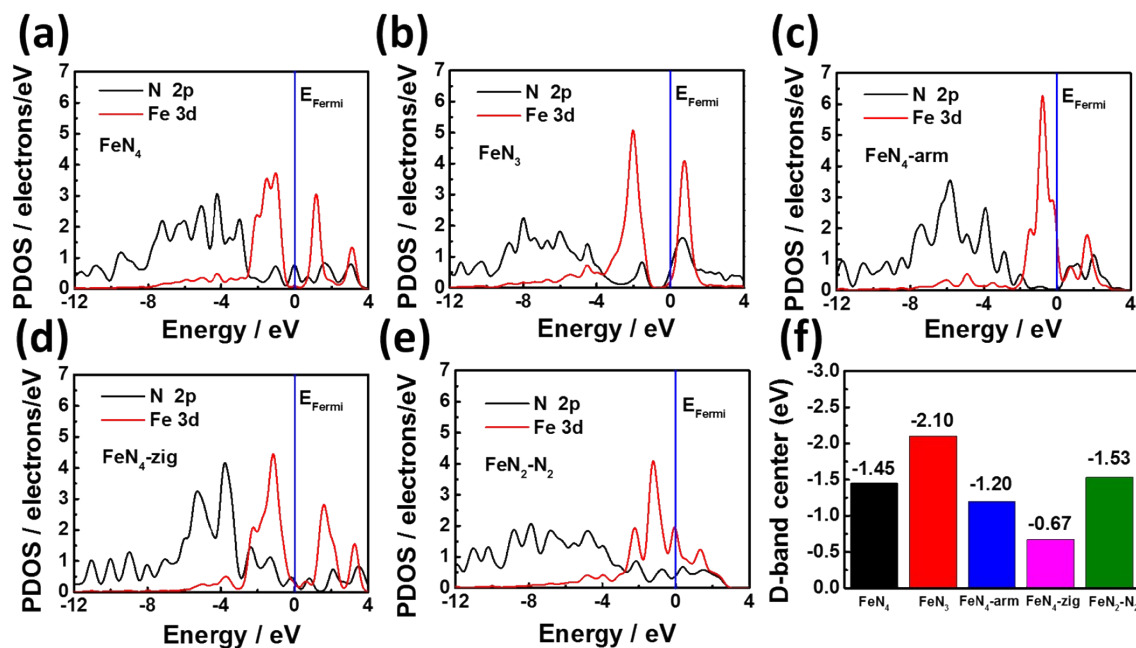
Figure S12. Partial density of state for Fe ion 3d and N 2p involved in (a) FeN_4; (b) FeN_3; (c) FeN_4-arm; (d) FeN_4-zig and (e) FeN_2-N_2; (f) Calculated d-band center of these active sites.
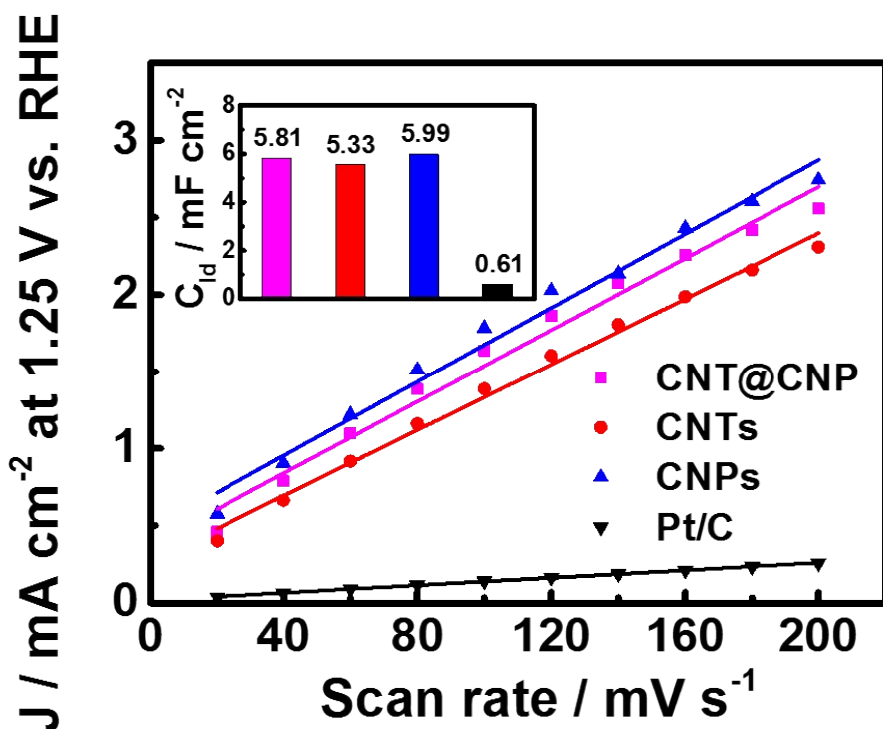
Figure S13. Current density in different scan rates at the fixed voltage of 1.25 V vs. RHE for CNT@CNP, CNTs, CNPs and commercial Pt/C (JM) under CV measurement.
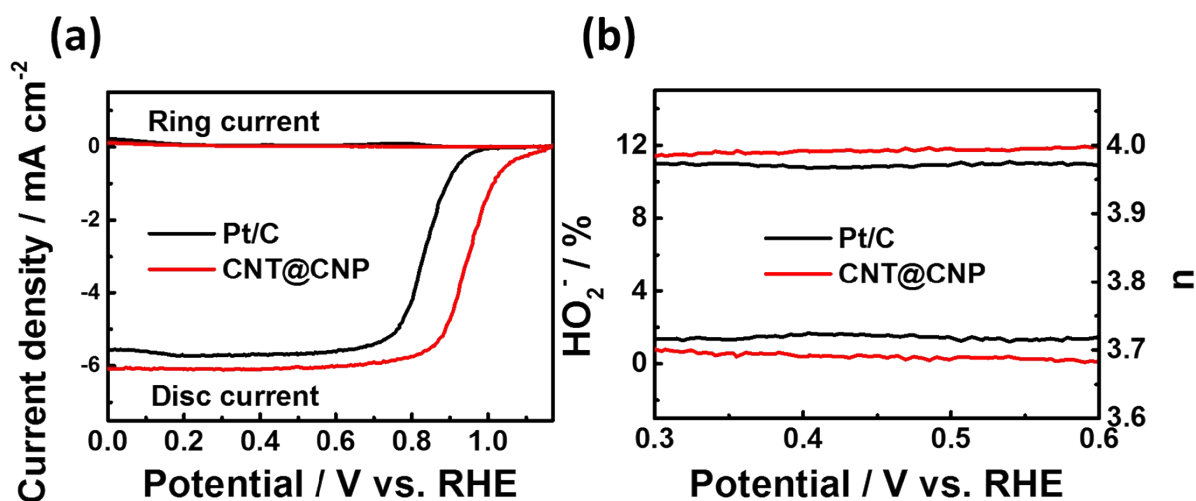
Figure S14. (a) Polarization plots of CNT@CNP interpenetrating networks and commercial Pt/C (JM) measured by RRDE test in the O_2-saturated 0.1 KOH solution with fixed rotating rate of 1600 rpm at 5 mV s^{-1}; (b) H_2O_2 yield and the numbers of electron transfer.
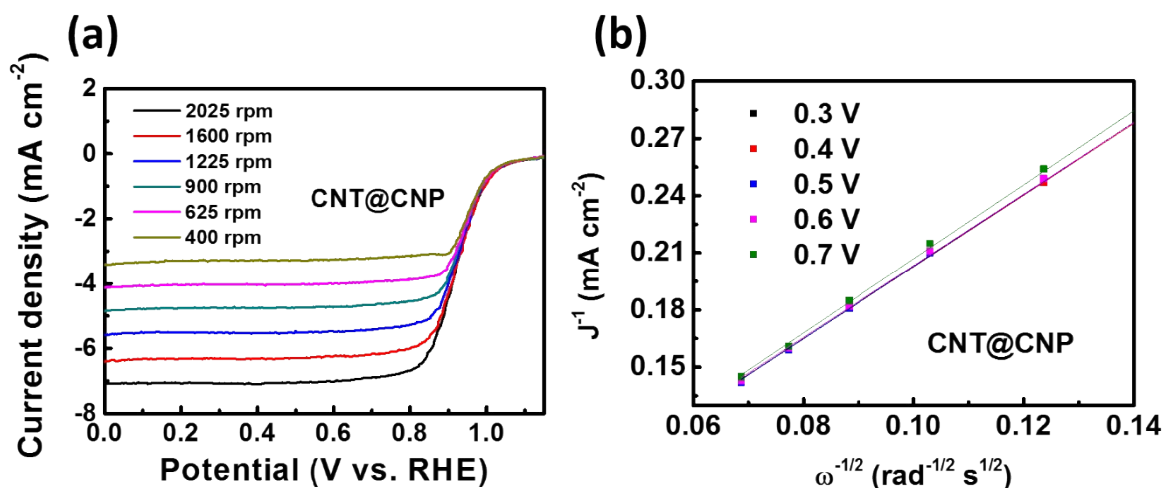
Figure S15. (a) LSV curve of CNT@CNP in 0.1 M KOH solution under different rotating speeds; (b) K−L curves at selected potentials derived from the LSV curves of CNT@CNP.
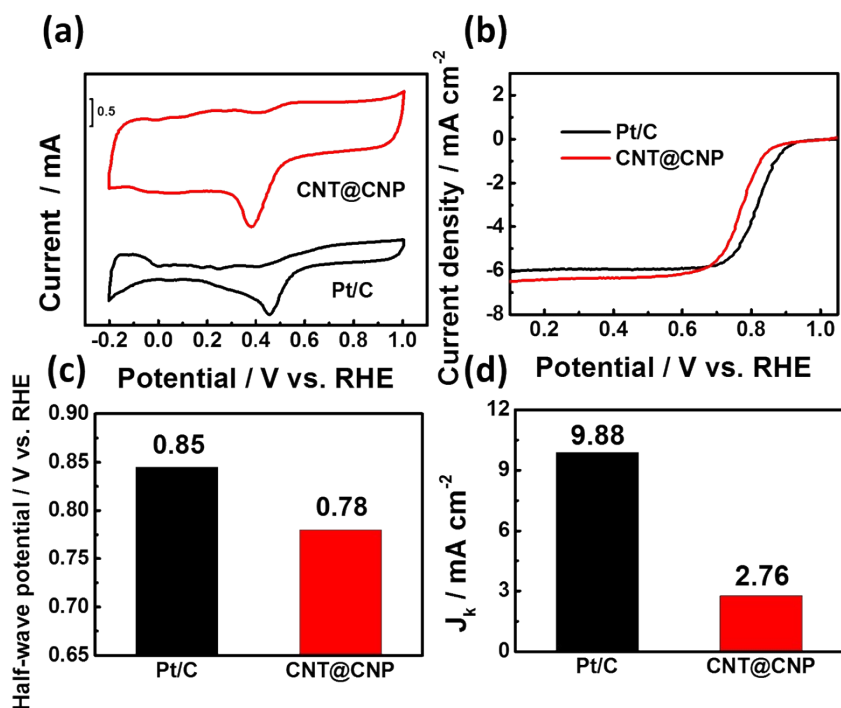
Figure S16. (a) CV curves of CNT@CNP and commercial Pt/C (JM) in O_2-saturated 0.1 M $HClO_4$ electrolyte, the scan rate was 20 mV s^{-1}. (b) Polarization curves of these samples above at a fixed rotation rate of 1600 rpm in 0.1 M $HClO_4$ solution with the scan rate at 5 mV s^{-1}; (c) Half-wave potential and (d) J_k at 0.8 V vs. RHE for these catalysts.
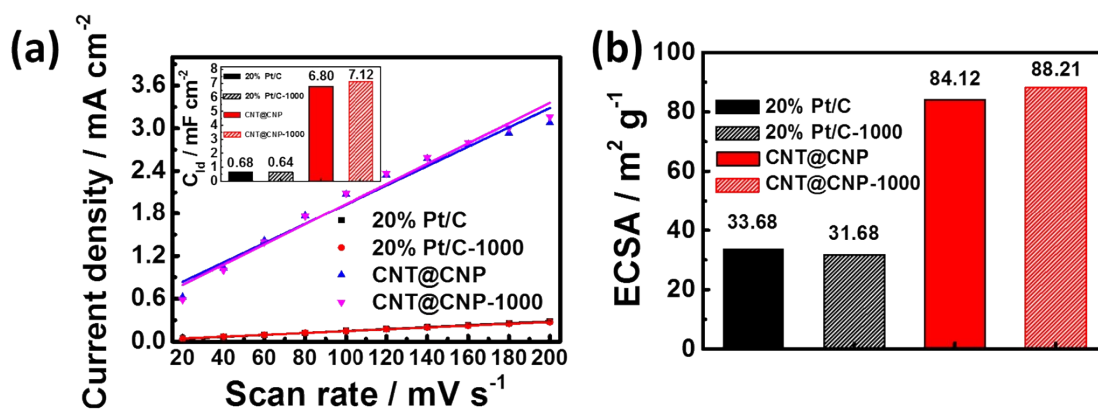
Figure S17. (a) Current densities at different scan rates at the fixed voltage of 1.25 V vs. RHE for CNT@CNP interpenetrating networks and commercial Pt/C (JM) under CV measurement. (b) ECSA of before and after 1000 cycles CV for these samples above.
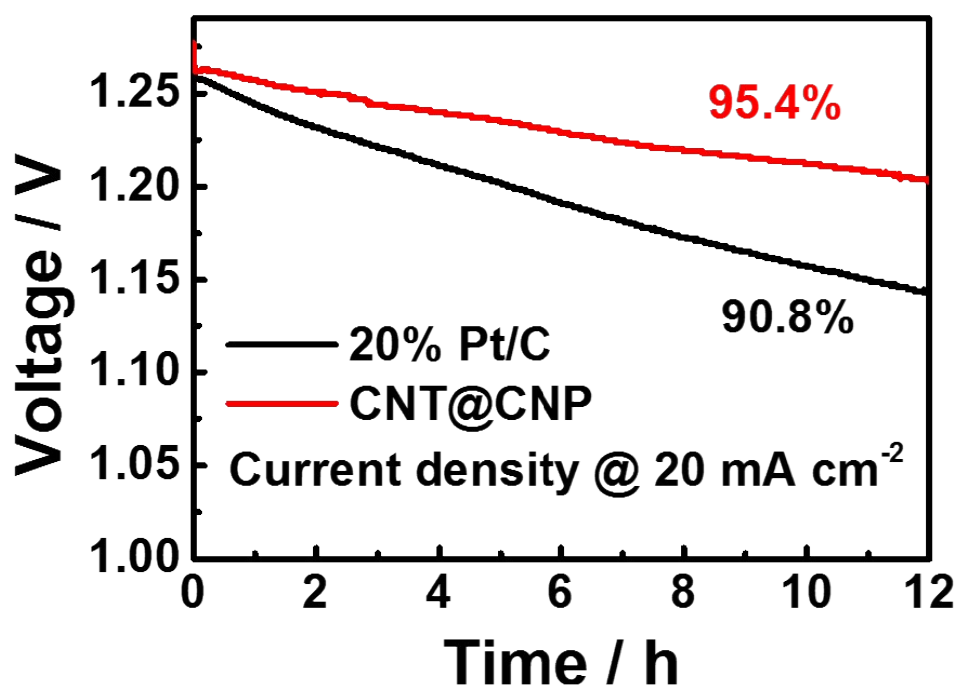

Figure S18. Discharging stability for CNT@CNP interpenetrating networks and commercial Pt/C (JM) at discharge current density of 20 mA cm^{-2}.

14
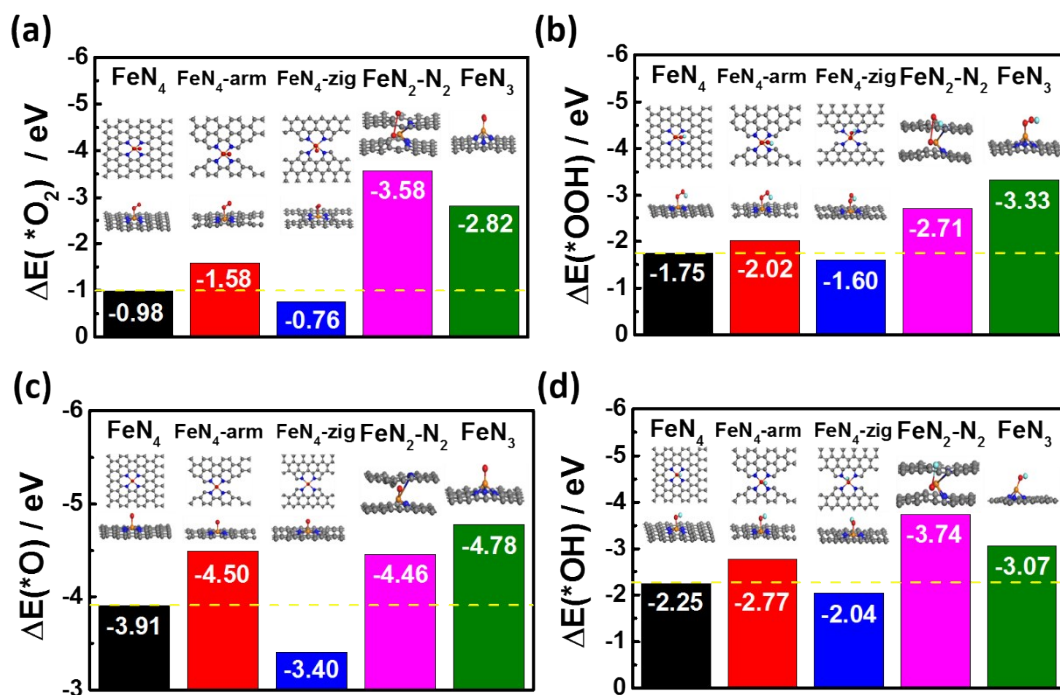
Figure S19. Different O-containing species adsorption energies, (a) $*O_2$, (b) $*OOH$, (c) $*O$ and (d) $*OH$ on different active sites including FeN_4, FeN_4-arm, FeN_4-zig, FeN_2-N_2 and FeN_3.

The calculated ΔE ($*O_2$) values for the edged FeN_4-arm, FeN_4-zig and FeN_2-N_2 are -1.58 eV, -0.76 eV, -3.58 eV respectively, as shown in Figure S17(a). Moreover, the ΔE ($*O_2$) of the FeN_4-zig is slightly more positive than that of the in-plane FeN_4 (-0.98 eV), while FeN_4-arm is little bit negative and both of them are much more positive than that of the in-plane FeN_3 (-2.82 eV). Figure S17(b)-(d) show the adsorption energy of $*OOH$, $*O$ and $*OH$ on the above sites, respectively. Among these moieties, the FeN_4-arm and FeN_4-zig exhibit the same order as in the adsorption energy of $*O_2$ compared with that of in-plane FeN_4 and FeN_3.
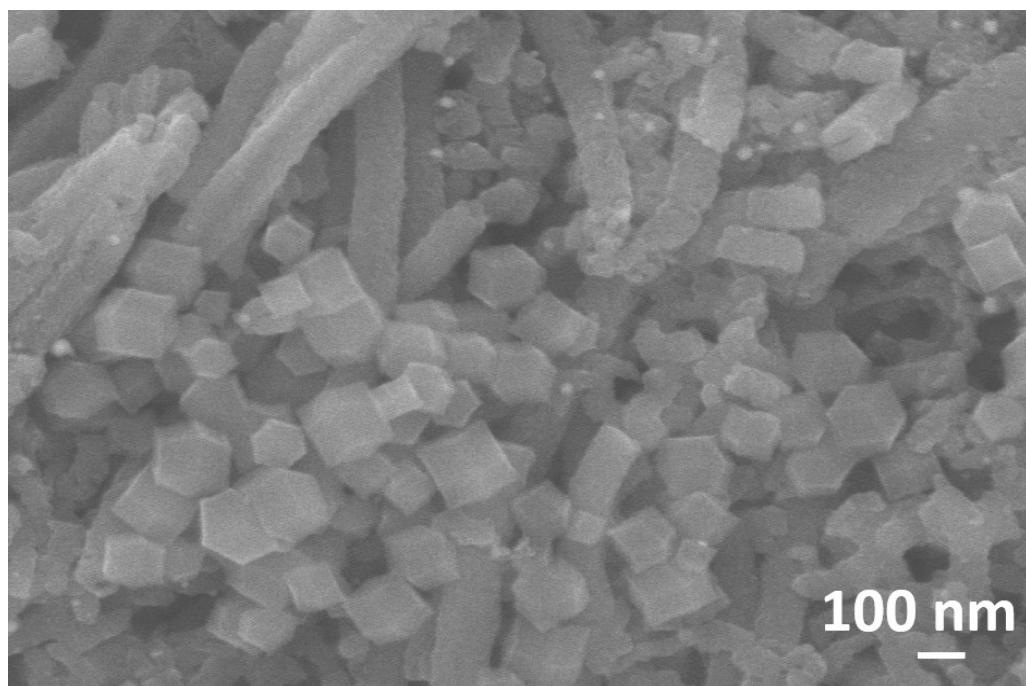
Figure S20. SEM image for CNT/CNP physical blend.
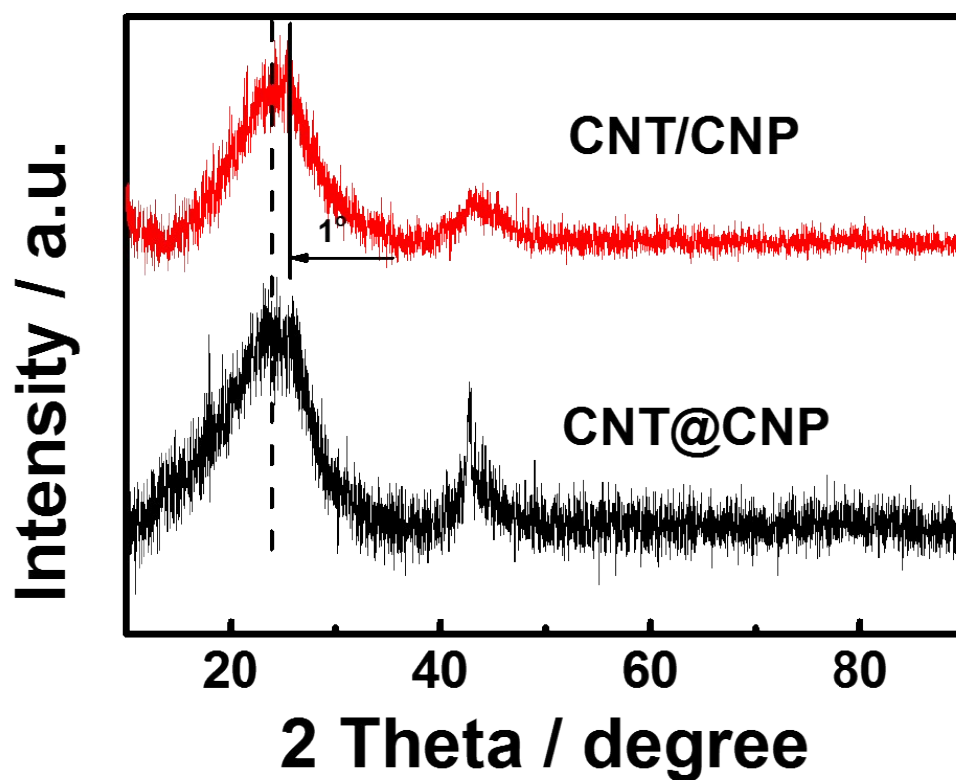
Figure S21. XRD spectra for CNT@CNP interpenetrating networks and CNT/CNP blend.
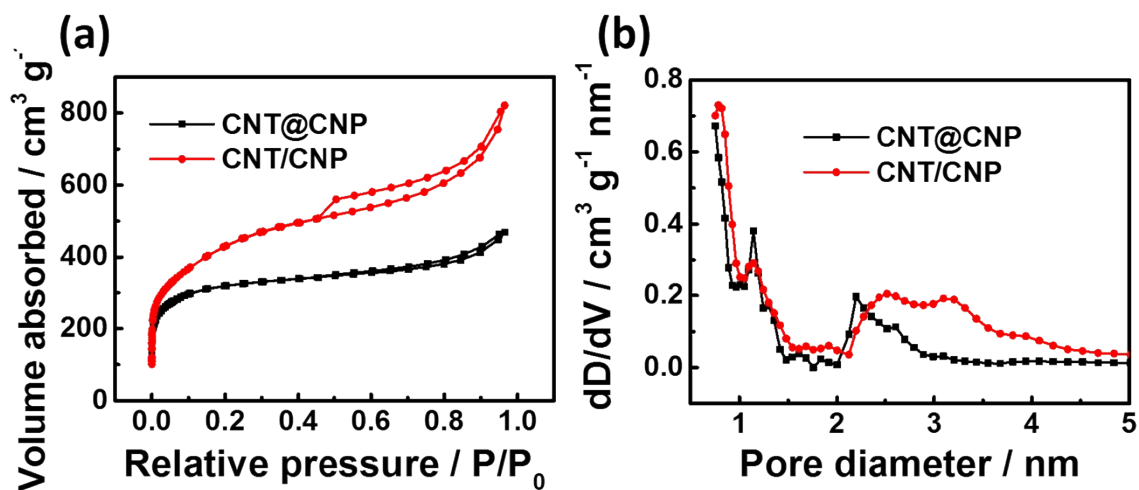
Figure S22. (a) N_2 adsorption-desorption isotherms and (b) Pore-size distributions as estimated by DFT method for CNT@CNP interpenetrating networks and CNT/CNP blend.
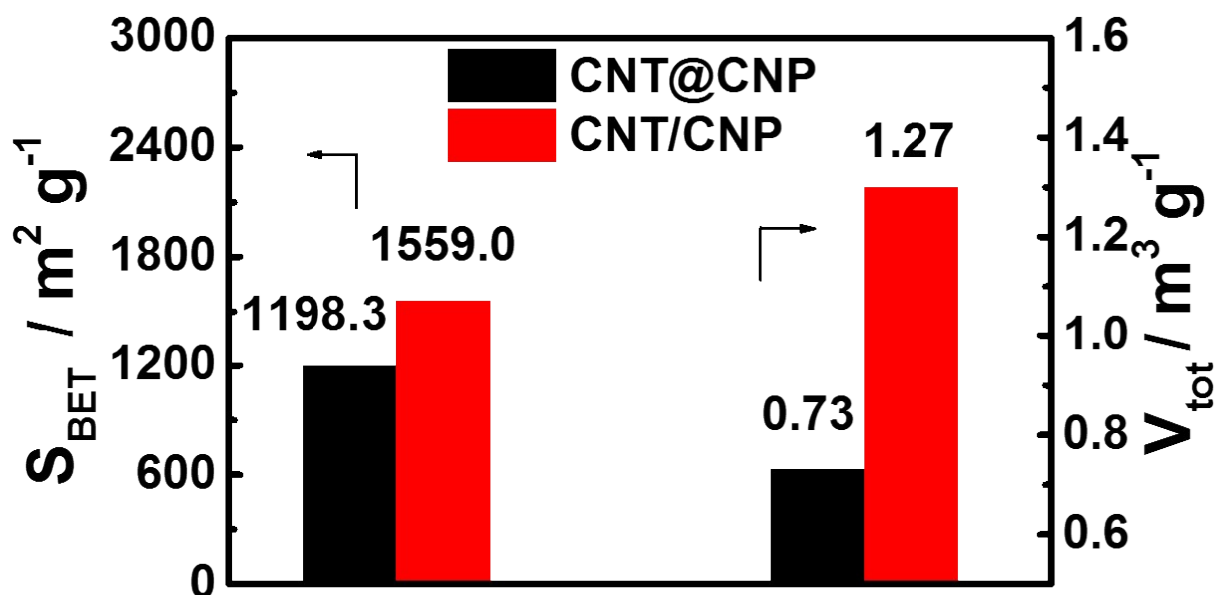
Figure S23. Calculated surface area and total pore volume for CNT@CNP interpenetrating networks and CNT/CNP blend .
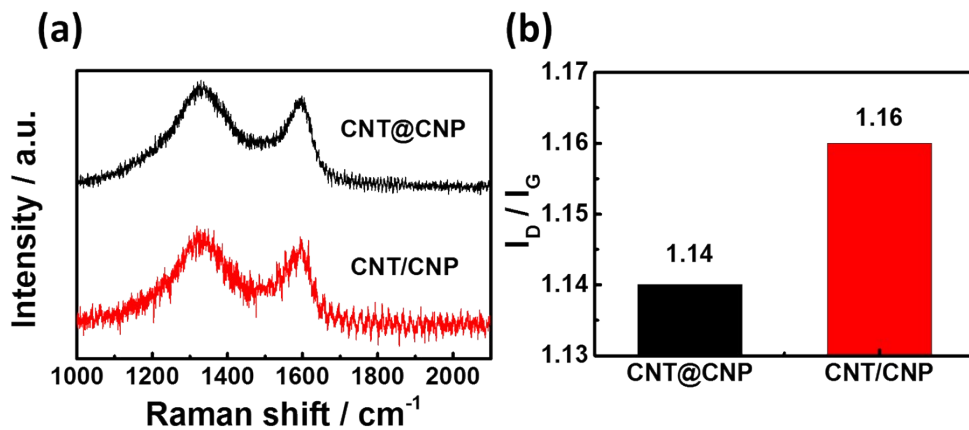
Figure S24. (a) Raman curves and (b) values of I_D/I_G for CNT@CNP interpenetrating networks and CNT/CNP blend.
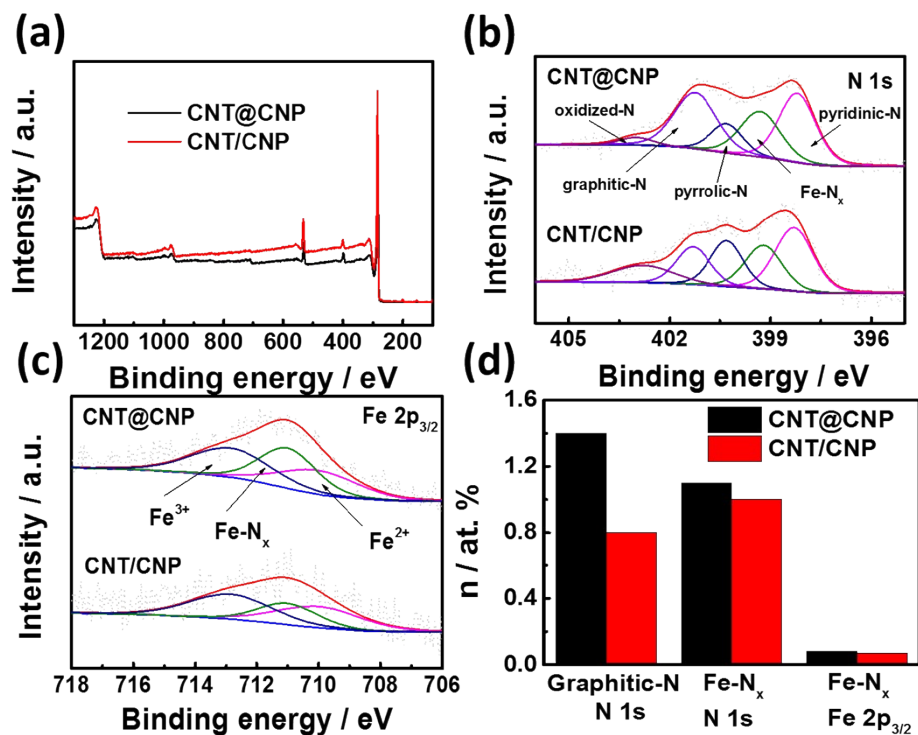
Figure S25. (a) XPS spectra surveys for CNT@CNP interpenetrating networks and CNT/CNP blend; the fitting XPS spectra of (b) N 1s and (c) Fe $2p_{3/2}$ for CNT@CNP and CNT/CNP; (d) Contents of graphitic-N and Fe-N$_x$ for CNT@CNP and CNT/CNP based on fitting result from N 1s and Fe $2p_{3/2}$.
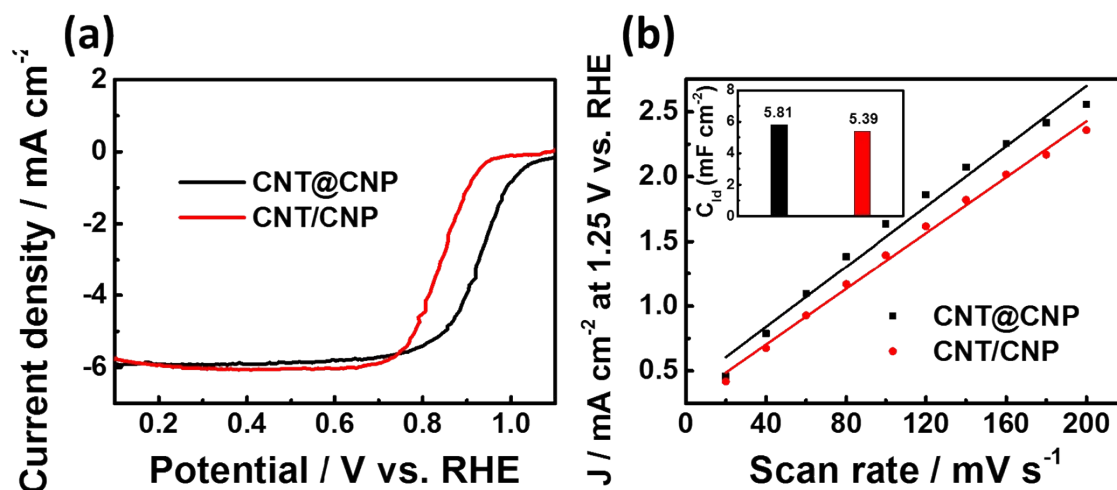
Figure S26. (a) Polarization curves of these samples above at a fixed rotation rate of 1600 rpm in 0.1 M KOH solution with the scan rate at 5 mV s^{-1} and (b) current density in different scan rates at the fixed voltage of 1.25 V vs. RHE under CV measurement for CNT@CNP interpenetrating networks and CNT/CNP blend.
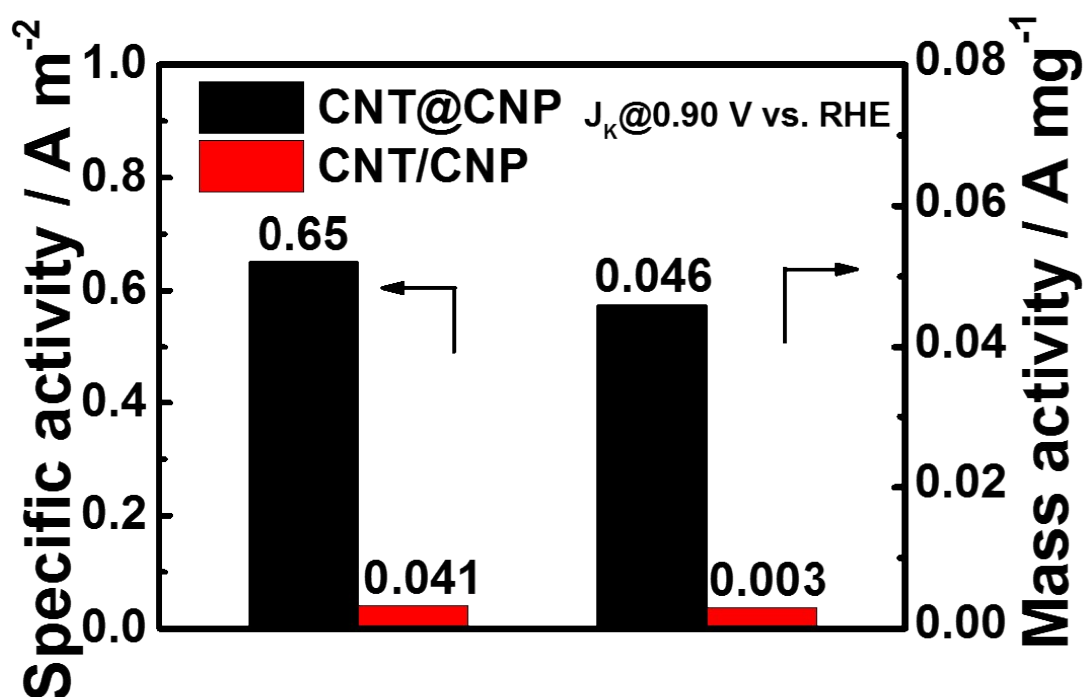
Figure S27. Mass activities and specific activities for CNT@CNP and CNT/CNP blend.

Tables

Table S1. Analysis of specific surface area and the distribution of pore structural parameters for the CNTs, CNPs, CNT@CNP interpenetrating networks and CNT/CNP blend.

Catalyst name	S_{BET} [m² g⁻¹]	S_{me} [m² g⁻¹]	S_{mi} [m² g⁻¹]	S_{me} / S_{mi} [%]	V_{tot} [cm³ g⁻¹]	V_{me} [cm³ g⁻¹]	V_{mi} [cm³ g⁻¹]	V_{me} / V_{mi} [%]
CNT@CNP	1198.30	201.12	997.18	0.83	0.73	0.32	0.41	0.56
CNTs	814.64	187.05	627.59	0.77	0.51	0.25	0.26	0.49
CNPs	1401.93	523.89	878.04	0.63	0.93	0.53	0.40	0.43
CNT/CNP	1559.05	1503.85	55.19	0.034	1.27	1.26	0.02	0.01

Table S2. The element weight ratio from XPS measurements for CNTs, CNPs, CNT@CNP interpenetrating networks and CNT/CNP blend.

Catalyst name	C [%]	N [%]	N/C [%]	O [%]	Fe [%]	Fe/C [%]
CNT@CNP	88.71	4.22	4.76	6.90	0.17	0.19
CNTs	89.61	5.90	6.58	4.36	0.13	0.14
CNPs	88.40	4.70	5.32	6.65	0.25	0.28
CNT/CNP	89.54	4.14	4.62	6.09	0.22	0.24

Table S3. The element atomic ratio of five nitrogen structures from XPS measurements for the CNTs, CNPs, CNT@CNP interpenetrating networks and CNT/CNP blend.

Catalyst name	Pyridinic N [at. %] 398.2 eV	Fe-N$_x$ [at. %] 399.3 eV	Pyrrolic N [at. %] 400.3 eV	Graphitic N [at. %] 401.3 eV	Oxidized N [at. %] 403.0 eV
CNT@CNP	1.02	0.94	0.79	1.12	0.89
CNTs	2.03	0.83	1.54	0.64	0.83
CNPs	1.50	1.10	0.55	1.42	0.15
CNT/CNP	1.54	1.00	0.95	0.81	0.68

Table S4. The element atomic ratio of three iron contents from XPS measurements for the CNTs, CNPs, CNT@CNP and CNT/CNP blend.

Catalyst name	Fe^{3+} [at. %] 712.85 eV	$Fe-N_x$ [at. %] 711 eV	Fe^{2+} [at. %] 710 eV
CNT@CNP	0.07	0.04	0.06
CNTs	0.06	0.02	0.06
CNPs	0.09	0.09	0.07
CNT/CNP	0.13	0.08	0.11

Table S5. Parameters of EXAFS fits for the CNT@CNP and Fe foil.

Catalyst name	Path	Coordination Number	Bond length R [Å]	Bond disorder σ^2 [10^{-3} Å^2]	R factor [%]
CNT@CNP (FeN$_4$)	Fe-N	4.0	1.86	0.0065	0.019
	Fe-C1	4.0	2.62	0.0073	
	Fe-C2	4.0	3.01	0.0036	
CNT@CNP (FeN$_3$)	Fe-N	4.0	1.66	0.0174	0.084
	Fe-C	6.0	2.05	0.0105	
Fe foil	Fe-Fe1	8.0	2.50	0.0078	0.0011
	Fe-Fe2	6.0	2.85	0.0176	

Table S6. Binding energies of FeN$_4$, FeN$_4$-arm, FeN$_4$-zig, FeN$_3$, FeN$_2$-N$_2$, N$_2$FeN$_2$, N-FeN$_{2+2}$ and FeN$_{4+1}$ for Fe ion included (E$_{FeNC}$) and Fe ion removed (E$_{NC}$) and their differences energy (E$_b$) when Fe inserted.

	E$_{FeNC}$ [eV]	E$_{NC}$ [eV]	E$_b$=E$_{FeNC}$-E$_{NC}$-E$_{Fe}$ [eV]
FeN$_4$	-456.05	-453.54	-1.75
FeN$_3$	-241.21	-237.96	-2.49
FeN$_4$-arm	-276.48	-273.54	-2.18
FeN$_4$-zig	-356.53	-352.11	-3.67
FeN$_2$-N$_2$	-462.00	-458.02	-3.21
N$_2$FeN$_2$	-458.58	-458.06	0.24
N-FeN$_{2+2}$	-694.72	-694.68	0.72
FeN$_{4+1}$	-482.72	-482.33	0.38

Table S7. The calculated electrochemical data of C_{ld}, ECSA, MA and SA for commercial Pt/C (JM), CNTs, CNPs, CNT@CNP interpenetrating networks and CNT/CNP blend.

Catalyst name	C_{ld} [mF cm^{-2}]	ESCA [m^2 g^{-1}]	MA [A mg^{-1}]	SA [A cm^{-2}]
Pt/C	0.61	30.13	0.0089	0.295
Pt	-	70	0.0445	0.635
CNT@CNP	5.33	65.82	0.0061	0.093
CNTs	5.99	73.97	0.0081	0.109
CNPs	5.81	71.75	0.0468	0.652
CNT/CNP	5.39	77.31	0.0032	0.041

Table S8. The calculated electrochemical data of C_{ld}, ECSA, MA and SA for commercial Pt/C (JM), CNT@CNP and those electrochemical data for these catalysts after 1000 CV cycles measurement, marked Pt/C-1000 and CNT@CNP -1000, respectively.

Catalyst name	C_{ld} [mF cm^{-2}]	ESCA [m^2 g^{-1}]	MA [A mg^{-1}]	SA [A cm^{-2}]
Pt/C	0.68	33.68	0.0042	0.125
Pt/C-1000	0.64	31.68	0.0012	0.038
CNT@CNP	6.80	84.12	0.0493	0.586
CNT@CNP-1000	7.12	88.21	0.0442	0.501

Table S9. Value used for binding energy, the entropy (at T=298.15 K) and zero-point energy corrections in determining the free energy reactants, products, and intermediate species adsorbed on catalysts. For the surface bound species, the ZPE values are averaged over model structures.

T=298.15 [K]	O_2* E_b [eV]	* E_b [eV]	ZPE [eV]	$T\Delta S$ [eV]	OOH* E_b [eV]	ZPE [eV]	$T\Delta S$ [eV]	O* E_b [eV]	ZPE [eV]	$T\Delta S$ [eV]	OH* E_b [eV]	ZPE [eV]	$T\Delta S$ [eV]
FeN$_4$	-463.79	-456.05	9.63	1.07	-466.77	10.13	1.32	-459.85	9.75	1.19	-463.26	9.97	1.24
FeN$_3$	-284.83	-276.84	5.72	0.93	-287.88	6.26	1.05	-280.87	5.81	0.99	-284.57	6.10	1.05
FeN$_4$-arm	-364.07	-356.53	7.30	1.07	-367.12	7.74	1.33	-359.84	7.32	1.15	-363.54	7.60	1.20
FeN$_4$-zig	-472.35	-461.99	9.86	1.14	-473.69	10.37	1.24	-466.35	9.94	1.21	-470.69	10.36	1.26
FeN$_2$-N$_2$	-250.81	-241.21	5.18	0.57	-253.52	5.67	0.73	-245.89	5.24	0.66	-249.24	5.51	0.65

Table S10. Binding energies for H_2, H_2O, O_2, OH, OOH, O and Fe, entropy (at T= 298.15 K) and zero-point energy for H_2, H_2O.

T=298.15 [K]	E_b [eV]	ZPE [eV]	$T\Delta S$ [eV]
H_2	-0.316	0.281	0.421
H_2O	-4.607	60.578	0.603
O_2	-6.775		
OH	-4.964		
OOH	-8.979		
O	0.0974		
Fe	-0.756		

Table S11. Reaction free energy of elementary step for four-electron transfer ORR on different FeN_4-type active sites of catalysts at output potential of 0, 0.9 and 1.23 V.

	Applied potential [V]	G(OOH*) [eV]	G(O*) [eV]	G(OH*) [eV]	ΔG_1 [eV]	ΔG_2 [eV]	ΔG_3 [eV]	ΔG_4 [eV]	U_{orr}^{onset} [V vs. RHE]
FeN_4	U=0	3.89	2.19	1.33	-1.02	-1.70	-0.86	-1.33	0.86
	U=0	3.72	1.96	0.89	-1.20	-1.76	-1.07	-0.89	0.89
FeN_4-arm	U=0.90	1.02	0.16	-0.01					
	U=1.23	0.03	-0.5	-0.34					
	U=0	3.96	2.63	1.54	-0.96	-1.33	-1.09	-1.54	0.96
FeN_4-zig	U=0.90	1.22	0.83	0.64					
	U=1.23	0.27	0.17	0.31					
FeN_2-N_2	U=0	3.09	1.64	0.05	-1.83	-1.45	-1.59	-0.05	0.05
FeN_3	U=0	2.39	1.28	0.60	-2.53	-1.10	-0.68	-0.61	0.61

Experiment:

The preparation procedure of CNT@CNP interpenetrating networks have been shown as following steps: Firstly, nitrogen-rich polyaniline (PANI) nanotubes structure-oriented template materials with high aspect ratio were synthesized, highly porous metal organic frameworks (MOF, ZIF-8) served as the second phase particles next has been uniformly inserted onto the PANI nanotubes network template through epitaxial method. The final CNT@CNP interpenetrating networks are obtained following the in-situ pyrolysis carbonization.

The preparation of polyaniline nanotubes as structure-oriented templates

Firstly, the main aqueous phase synthesis method has been carried out in this work. We have used aniline (AN) as monomer material, succinic acid as doped acid and ammonium persulfate (APS) as initiator to directly obtain the polyaniline (PANI) nanotubes under accurately regulating the temperature of the reaction system. The influences of monomer concentration, doped acid, the type and concentration of initiator, addition mode and other synthesis conditions on the morphology and structure of PANI were systematically studied. Based on the analysis above, the nanotubes with high aspect ratio were prepared. The polyaniline nanotubes (about 1-2 μm in length) with high aspect ratio, as well as, 100-150 nm pipe diameter and 60 nm wall thickness have been prepared through the best synthesis conditions were as follow: 0.5904 g succinic acid as a doped acid was dissolved in 100 mL with fully ultrasonic agitation. The obtained solution was evenly divided into two parts, one of them was added 2.282 g APS (99%), the other was injected in 0.913ml AN. Both of these mixed solutions should stir well and place them in the temperature of 5℃ for 30 min. After that the APS solution quickly pour into the AN liquid at the low reaction temperature for 14 h reaction

time. The precursor PANI was obtained after filtration of water and alcohol washed and put into dry oven set 70℃ for 10 h.

The preparation of dual carbon interpenetrating networks

Secondly, using the prepared PANI as a structure-oriented template, ZIF-8 dodecahedron structures are diffusely embedded in the polyaniline nanotubes network in the form of second-phase particles through epitaxial growth. The specific synthesis process is as follows: transfer the polyaniline nanotubes mentioned above to methanol solution, select imidazole as organic ligands, and build ZIF-8 materials with transition metal iron chlorides ($FeCl_3$) as central metal atoms. In the nucleation stage of ZIF-8, there are large amounts of hydrogen bond or cyano functional group existed between small molecules imidazole and PANI, the coordination among these bond or functional groups could induce the nucleation and extension growth of ZIF-8 on the PANI nanotubes surface. These dodecahedral structures in the form of second phase particles, therefore, dispersed in polyaniline nanotubes networks. For the prepared process details: we put 400 mg PANI (percusor), 1.95 g $Zn(NO_3)_2 \cdot 6H_2O$ and 10.6 mg $FeCl_3$ into 80 mL methanol (99%) with agitation marked A solution. In addition, 2.15 g 2-Methylimidazole was add into the other 80 mL methanol following ultrasonic mixture labeled B liquid. The B liquid was quickly poured into A solution under magnetic stirring for 3 h and static settlement for 24 h. the final PANI@ZIF-8 was form after filtration and dry process at 70℃ for 10 h. in order to get the carbon-carbon network catalyst CNT@CNP, the precursor should be carbonized under 400℃ in Ar atmosphere for 1 h and high-temperature activating pyrolysis at 900℃ for 2 h with a heating rate of 5℃/min. For accounting for and comparing the ORR activity of the hybrid with each composition, every monomer (labeled as CNTs and CNPs, respectively) as a control trail has been prepared by same method. Thirdly, by regulating the relative content of polyaniline nanotubes and ZIF-8 nanoparticles, the influence of the

compositions of PANI@ZIF-8 hybrids on the hybrid nano-phase structure was investigated, and the formation mechanism of PANI/ZIF-8 two-phase composites with typical topological network extension structure was proposed. Therefore, a simple mechanical mixture material of CNTs and CNPs has been prepared as comparison, which is marked as CNT/CNP blend.

Characterization:

X-ray diffraction (XRD) patterns of PANI@ZIF-8, ZIF-8, CNTs, CNPs, CNT@CNP interpenetrating networks, and CNT/CNP blend were acquired by a scan rate of 5 per minute in the range from 10° to 90° (Rigaku RINT 2200 V/PC). For determining the loadings of CNTs and CNTs on the carbon catalyst, thermogravimetric-differential thermal analysis (TG-DTA) was carried out on a Rigaku TG-8120 with a heating rate of 5 K min^{-1} under an air atmosphere to determine the loading contents of each monomer phase. The scanning electron microscopy (SEM) (FE-SEM, JEOL, JSM-6701F) and high resolution transmission electron microscopy (TEM) (JEOL TEM 2010 microscope) had examined morphologies of the samples. The graphitization degree of the synthesized samples was performed by Raman spectra (Horiba Jobin Yvon LabRam HR800). In addition, Quadrasorb SI (Quantachrome Instruments) with calculated method of Quenched solid density functional theory (QSDFT) was used for obtaing the Brunauer−Emmett−Teller (BET) specific surface area and pore structure. To confirm the surface structure of the catalyst for all the samples above, X-ray photoelectron spectroscopy (XPS, Thermo ESCALAB 250), where the Lorentzian-Gaussian parameter was fixed at 20 %, was put into service. For more accurate detail information, The X-ray absorption near-edge structure (XANES) region and extended X-ray absorption fine structure (EXAFS) region were therefore obtained and analyzied. X-ray absorption spectra (XAS) at K-edge was recorded at the beam line 1W1B of the Beijing Synchrotron Radiation Facility (BSRF, China). The typical energy of the storage ring was 2.5 GeV in BSRF with maximum current of 250 mA. EXAFS

data were collected using a fixed-exit Si (111) double crystal monochromator, and then the collected XAFS data was measured in transmission mode for the reference spectrum. The XAS data at Fe K-edges of CNT@CNP interpenetrating networks, iron phthalein cyanide (FePc) and Fe foil were extracted and processed according to the standard procedures using the ATHENA module implemented in the IFEFFIT software package.

Electrochemical tests:

Catalysts of CNT@CNP, CNTs, CNPs, CNT/CNP and commerical Pt/C (JM) were measured through a rotating disk machine (AFCBP1 type, PINE, USA) with typical three electrodes system to obtain the oxygen reaction reduction electrocatalytic activity. The counter electrode in that three electrodes system is graphite, while the saturated calomel electrode (SCE) is used as reference electrode in this work. All electrochemical tests were managed in 0.1 M KOH with oxygen saturated electrolyte. The carbon catalyst ink of the sample is prepared by dispersing 5 mg catalyst in 1 ml alcohol and 20 μl Nafion solution (5 wt %) for 30 minutes by ultrasonically dispersing. 20 μl of the electrocatalyst ink has been dropped evenly on the surface of rotating disk electrode (S_{disk} = 0.247 cm^2) for all the carbon catalysts, while 5μl is applied to commercial Pt/C catalyst (JM). After the ethanol volatilized at room temperature, the final work electrode will form. For the cyclic voltammetry (CV) test, all the catalysts were tested under a scanning rate of 20 mV s^{-1}, while the rate applied to polarization curve in the rotating ring and disk electrode (RRDE) experiments is 5 mV s^{-1}. The catalytic durability was aquired by accelerated durability test (ADT) with a fixed potential range from 0.008 to 1.109 V vs. RHE and a scan rate of 100 mV s^{-1} in O$_2$-saturated 0.1M KOH solution for 1000 CV cycles. The potentials of all these work above were normalized with respect to the reversible hydrogen electrode (RHE). The potential vs. RHE ($E_{vs.RHE}$) was calculated by the following equation:

$$E_{vs.RHE}=E_{vs.SCE}+0.241+0.059pH \tag{S2}$$

Where $E_{vs.SCE}$ stands for the potential vs. SCE.

The electron transfer number (n) and the kinetic current (jk) performed in oxygen reaction reduction were aquired by the Koutecky-Levich (K-L) plots. The K-L equation calculated n value of in the range of 0.3-0.7 V based on the RDE curves through rotating disk electrode (RDE) system at different rotating rates in 0.1 M KOH. In addition, The n obtained by RRDE results in the scanning range of 0.3-0.6 V. Moreover, the hydrogen peroxide yield (H_2O_2%) was obtained by equation below from RRDE measurement. The H_2O_2% and n computational formula from RRDE system and K-L equations for calculating n and j_K are shown below:

$$H_2O_2\% = (200I_R/n_0) / (I_R/n_0+I_D) \tag{S3}$$

$$n = 4I_D / (I_R/n_0+I_D) \tag{S4}$$

$$1/j = 1/j_K +1/j_L = 1/B\omega^{1/2} + 1/j_K \tag{S5}$$

$$B = 0.62nFC_0D_0^{2/3}v^{-1/6} \tag{S6}$$

$$j_K =nFkC_0 \tag{S7}$$

From the equation above, the I_R represents ring current, I_D denotes as disk current and n_0 defines as the disk current collection efficiency of the machine is a constant value (0.37). Moreover, j represents current density, j_K and j_L are served as kinetic current densities and the limiting diffusion current densities, respectively. D_0 is the O_2 diffusion coefficient, ω is called electron rotating rate, k is denoted as the electron transfer rate constant, and v is kinematic viscosity. n and C_0 in the equations of B are termed as the electrons transferred number and bulk concentration of oxygen, respectively. F is defined as the Faraday constant (96485 C mol^{-1}).

In addition, the electrochemical surface areas of catalysts were calculated from the result of CV measurement. Catalysts were tested under different rotated rate from 20 to 200 mV s^{-1} in

0.1 M KOH oxygen saturated solution. The current densities at 1.25 V vs. RHE (in this work) have been selected as Y-axis with X-axis of different rotated rate to make a figure. Half value of the graphic slope was then divided by electrical double-layer capacitor 20 μF cm^{-2}, as called RF. The ECSA value was obtained from RF per mass weight. Therefore, mass and specific activity under LSV experimental test of 5 mV s^{-1} are calculated as below:

Mass activity (A mg^{-1}) = 10^{-3} * J_k (@0.9 V vs. RHE, mA cm^{-2}) * S_{disk} (cm^2) / m_{cat} (mg)   (S8)

Specific activity (A cm^{-2}) = 10 * Mass activity (A mg^{-1}) / $ECSA_{cat}$ (m^2 g^{-1})   (S9)

Where J_k represents the kinetic current density at potential of 0.9 V vs. RHE, S_{disk} is 0.247 cm^2 defined as surface area of electrode disk and m_{cat} denotes as mass of relevant catalyst. The $ECSA_{cat}$ in specific activity is called as electrochemical surface area calculated by CV test at different scanning rates.

Moreover, methanol tolerance tests were performed by chronoamperometric cures with addition of 5 % methanol at around 300 s during the ORR.

Zn-air Battery test:

The dischargeable Zn-air battery experiments were carried out through the home-made battery. The cathode was prepared by dropping ink catalyst of CNT@CNP and Nafion liquid on a carbon paper (1.7*1.7 cm^2, effective reaction area 1.13 cm^2) and dried at 60 ℃ for 2 h (1.0 mg cm^{-2}). The zinc piece was used as the anode electrodes. Both electrodes were assembled into the home-made battery with 6 M KOH aqueous solution being used as electrolyte. The rate capability of discharge process was performed in different current density of 1, 2, 5, 10, 20, 40 and 1 mA cm^{-2}. The stability of discharge of CNT@CNP and commercial Pt/C (JM) was carried out at 20 mA cm^{-2} for 12 h. In addition, rechargeable Zn-air battery test has been operated in the 6 M KOH and 0.2 M Zn(Ac)$_2$ solution with Zn piece and the mass loaded of CNT@CNP

and IrO_2 (20 wt. %) is 0.5 mg cm^{-2} for air cathode on carbon paper, respectively. The measurements run 60 circles, 10 min for a charging and discharging circle.

DFT calculation:

The calculations of geometry optimization and total energy proprieties are carried out by using first-principle calculations within the framework of density functional theory (DFT), as implemented in the plane wave set Materials Studio (MS).[9] The Perdew-Burke-Ernzerhof (PBE) functional[10] within the generalized gradient approximation (GGA) was used to model the exchange correlation energy. The projector augmented wave (PAW) pseudo-potentials[11] were used to describe the interaction valence electron and ionic cores. The core electrons for the doped metal atomsare treated by DFT Semi-core Pseudopot. The basis sets were adopted double numericalplus polarization (DNP) with a real-space global orbital cutoff radius of 3.0 Å. The convergence criteria forstructure optimizations were set as energy tolerance of $2.72 * 10^{-4}$ eV per atom, maximum force tolerance of 0.0544 eV/Å and maximum displacement tolerance of $5.0 * 10^{-3}$ Å. The converged criterion of self-consistent field (SCF) is within $2.72 * 10^{-5}$ eV per atom. In order to avoid their interactions between the graphene sheets, A sufficiently large vacuum space in the z-directionwas was set to 15 Å,. After fully relaxed aquired by DMol3, all of the structures are subjected to densities of states (DOS) are obtained on a Monkhorst-Pack grid with the 4*4*1 k-points for FeN_4 and FeN_3, 4*3*1 k-points for FeN_4-arm, 3*3*1 k-points for FeN_4-zig and 4*4*2 k-points for FeN_2-N_2, N_2FeN_2, $NFeN_{2+2}$ and FeN_{4+1}.

Reaction mechanism:

The ORR activities on active sites of various electrocatalysts were studied in details according to the electrochemical framework developed by Nørskov and his co-workers[12] As for ORR, O_2 is reduced either through a two-electron process, or completely via a direct four-electron pathway. In an alkaline electrolyte (pH= 14), H_2O rather than H_3O^+ may act as the proton donor, so the overall reaction scheme of the four-electron transfer ORR can be written as:

$$O_2 + 2H_2O + 4e^- \leftrightarrow 4OH^- \tag{S10}$$

The four-electron transfer ORR may proceed through two possible mechanisms: the associative pathway that involves protonation of O_2 or a direct O_2 dissociation pathway. The associative mechanism can be split into the following elementary steps which are usually employed to investigate the electrocatalysis of the ORR on various materials:

$$O_2(g) + H_2O(l) + e- \rightarrow OOH^* + OH- \tag{S11}$$

$$OOH^* + e- \rightarrow O^* + OH- \tag{S12}$$

$$O^* + H_2O(l) + e- \rightarrow OH^* + OH- \tag{S13}$$

$$OH^* + e- \rightarrow OH- + * \tag{S14}$$

Where * represent for an active site on the catalytic surface, (l) and (g) refer to liquid and gas phases, respectively, and O*, OH* and OOH* are adsorbed intermediates.

In alkaline solution, a four-electron pathway of ORR on an active site starts from adsorption energies of the O_2 molecule, undergoes a series of elementary reactions involving OOH, O and OH, following the ends with desorption of OH$^-$. Therefore, the adsorption energies of the ORR species (O_2, OOH, O and OH) on the active site of computational modules are calculated by:

$$\Delta E\ (^*O_2) = E\ (O_2{}^*) - E\ (^*) - E\ (O_2) \tag{S15}$$

$$\Delta E\ (^*OOH) = E\ (OOH^*) - E\ (^*) - E\ (OOH) \tag{S16}$$

$$\Delta E\ (^*O) = E\ (O^*) - E\ (^*) - E\ (O) \tag{S17}$$

$$\Delta E\ (^*OH) = E\ (OH^*) - E\ (^*) - E\ (OH) \tag{S18}$$

Reaction free energy:

Reaction free energies are approximate values of activation barriers for proton-transfer steps. [13] It qualitatively represent the right relative energetic ordering of a given proton-transfer elementary steps, though this approximation may result in a slight overestimation of activity for a given proton-transfer elementary step. Therefore, derived thermochemistry for ORR reactions (S8)-(S11) have been taken. The electron/proton transferred Gibbs reaction free energy of these electrochemical elementary steps based on using density functional theory (DFT) calculations and the computational normal hydrogen electron (NHE) model developed by Nørskov and co-workers was involved.[12][14-15] In this model, the calculation of reaction free energy is perform by setting up NHE as the reference electrode, which allows us to replace chemical potential with that of half a hydrogen molecule at standard conditions (U = 0 V vs. NHE, pH = 0 bar, T = 298 K). In order to obtain the reaction free energy of each elementary step in ORR on different sites for various model electrocatalysts, we calculate the adsorption free energy of O*, OH* and OOH*. because the exact free energy of OOH, O, and OH radicals in electrolyte solution is difficult to obtain, the adsorption free energies ΔG_{OOH*}, ΔG_{O*} and ΔG_{OH*} are relative to the free energy of stoichiometrically appropriate amounts of H_2O (g) and H_2 (g), defined as below:

$$\Delta G_{OOH*} = E_{OOH*} + 1.5 \times E_{H2} - 2 \times E_{H2O} + \Delta ZPE - T \times \Delta S \tag{S19}$$

$$\Delta G_{O*} = E_{OOH*} + E_{H2} - E_{H2O} + \Delta ZPE - T \times \Delta S \tag{S20}$$

$$\Delta G_{OH*} = E_{OOH*} + 0.5 \times E_{H2} - E_{H2O} + \Delta ZPE - T \times \Delta S \tag{S21}$$

Where zero-point energy (ZPE) was obtained by fixing the model electrocatalysts when calculating the vibrational frequencies of adsorbed species (O*, OH* and OOH*). T is the temperature and ΔS is the entropy change. Entropy values of gaseous molecules are taken from the standard tables in the Physical Chemistry test book.[16] However, the entropies of intermediates adsorbed on clusters plays a slight role.

For each elementary step, the Gibbs reaction free energy ΔG is defined as the difference between free energies of the initial and final states, which is given by the expression：

$$\Delta G = \Delta E + \Delta ZPE - T\Delta S + \Delta G_U + \Delta G_{pH} \tag{S22}$$

Where ΔE is the reaction energy of reactant and product molecules adsorbed on catalyst surface based on DFT calculations; ΔZPE and ΔS are the change of zero point energies and entropy derived from the reaction, respectively. The bias effect on the free energy of each initial, intermediate and final state involving an electron in the electrode should be considered through shifting the energy of the state by $\Delta G_U = -neU$, where e and n are the elementary charge transferred and the number of proton-electron pairs transferred, respectively. U is the electrode applied potential relative to NHE as mentioned above. Because of the effect of a pH different from 0 of the electrolytic solution, the change of free energy is taken into account by the correction for H^+ ions concentration ($[H^+]$) dependence of the entropy, $\Delta G_{pH} = -k_B T \ln[H^+] = pH \times k_B \ln[H^+]$, where k_B and T are the Boltzmann constant and the temperature, respectively. Therefore, the equilibrium potential U_0 of four-electron transfer ORR at pH=14 was determined to be 0.402 V vs. NHE or 1.23 V vs. RHE according to Nernst equation (E=E^0-0.0591pH, U^0_{RHE} = U^0_{NHE} +0.828 = 1.23 V), where the reactant and product are at the same energy level. Because of the oxygen molecule is poorly described in DFT calculations when given in the high-spin ground state, the free energy of the O_2 molecule was derived according to $G_{O2}(g) = 2G_{H2O}(l) - 2G_{H2} + 4 \times 1.23$ (eV). The free energy of OH^- was derived as $G_{OH^-} = G_{H2O}(l) - G_{H+}$, where G_{H+} = $1/2G_{H2}$ - $k_B T \ln 10 \times pH$. The free energy for gas phase water is calculated at 0.035 bars for the equilibrium pressure in contact with liquid water at 298 K. At these conditions, the free energy of gas phase water can be served as the free energy of liquid water.

The reaction free energy for four-electron transfer ORR can be expressed with the adsorption free energy of various oxygenated species, gas phase H_2 and H_2O defined earlier, which can show below:

$$\Delta G_1 = \Delta G_{OOH*} - 4.92 + eU + pH \times k_B T\ln10 \qquad (S23)$$

$$\Delta G_2 = \Delta G_{O*} - \Delta G_{OOH*} + eU + pH \times k_B T\ln10 \qquad (S24)$$

$$\Delta G_3 = \Delta G_{OH*} - \Delta G_{O*} + eU + pH \times k_B T\ln10 \qquad (S25)$$

$$\Delta G_4 = -\Delta G_{OH*} + eU + pH \times k_B T\ln10 \qquad (S26)$$

For ORR, the onset potential is calculated by the following equation:

$$U_{onset} = -\max\{\Delta G_1, \Delta G_2, \Delta G_3, \Delta G_4\} \qquad (S27)$$

References

[1] M. K. Liu, Y. F. Song, S. X. He, W. W. Tjiu, J. Pan, Y. Y. Xia, T. X. Liu, *Acs Appl. Mater. Inter.* **2014**, *6*, 4214.

[2] J. X. Jiang, F. Su, A. Trewin, C. D. Wood, H. Niu, J. T. A. Jones, *J. Am. Chem. Soc.* **2008**, 130, 7710.

[3] W. Yang, T. P. Fellinger, M. Antonietti, *J. Am. Chem. Soc.* **2011**, *133*, 206.

[4] W. Wei, H. W. Liang, K. Parvez, X. D. Zhuang, X. L. Feng, K. Müllen, *Angew. Chem., Int. Ed.* **2014**, *53*, 1570.

[5] M. Bayati, K. Scott, *Electrochim. Acta* **2016**, *213*, 927.

[6] C. Z. Wang , F. Yang , T. Qiu , Y. Cao, H. L. Zhong, C. C. Yu, R. J. Li, L. Q. Mao, Y. F. Li, *J. Electroanal. Chem.* **2018**, *810*, 62.

[7] Z.Y. Wu, X.X. Xu, B.C. Hu, H.W. Liang, Y. Lin, L.F. Chen, S.H. Yu, *Angew. Chem. Int. Ed.* **2015**, *54*, 8179.

[8] W. Niu, L. Li, X. Liu, N. Wang, J. Liu, W. Zhou, Z. Tang, S. Chen, *J. Am. Chem. Soc.* **2015**, *137*, 5555.

[9] B. Delley, *J. Chem. Phys.* **2000**, *113*, 7756.

[10] J. Perdew, K. Burke, M. Ernzerhof, *Phys. Rev. Lett.* **1996**, *77*, 3865.

[11] G. Kresse, D. Joubert, *Phys. Rev. B* **1999**, *59*, 1758.

[12] J. K. Nørskov, J. Rossmeisl, A. Logadottir, L. Lindqvist, J. R. Kitchin, T. Bligaard, *J. Phys. Chem. B* **2004**, *108*, 17886.

[13] S. K. Desai, M. Neurock, *Phys. Rev. B* **2003**, *68*, 1071.

[14] J. Rossmeisl, Z. Qu, H. Zhu, G. Kroes, J. Nørskov, *J. Electroanal. Chem.* **2007**, *607*, 83.

[15] J. Rossmeisl, A. Logadottir, J. K. Nørskov, *Chem. Phys.* **2005**, *319*, 178.

[16] J. De Paula, Atkins' Physical chemistry, Oxford University Press, **2010**.